

Unsteady Viscous/Inviscid Coupling Approaches for Propeller Flow Simulations

Katja Wöckner¹, Martin Greve¹, Martin Scharf¹, Thomas Rung¹, Moustafa Abdel-Maksoud¹

¹Institute for Fluid Dynamics and Ship Theory, Hamburg University of Technology, Germany

ABSTRACT

This paper reports the development and application of coupling strategies between viscous and inviscid propeller flow simulation techniques. The effort aims to combine the advantages of viscous and inviscid methods in order to reduce the computational cost compared to geometrically resolved viscous simulations.

The work has been performed under the aegis of the joint European co-laborative MARTEC project PROPSEAS, which is devoted to the analysis of seaway influences on propulsion systems. Attention is given to the resolution of inherently transient/dynamic processes, which require an adequate resolution of the individual blade motion and a time-resolving coupling strategy. Moreover, the free-surface has been included into the coupling procedure.

Applications refer to open-water predictions of experimentally investigated model-scale propeller flows and an unsteady podded propeller flow. Supplementary validation and verification cases, which outline the predictive performance and the computational efficiency of the employed strategies, are investigated.

Keywords

Viscous/inviscid-coupling, unsteady free-surface flows

1 INTRODUCTION

Reliable predictions of propulsion systems in seaways are of great interest for offshore operating vessels. Large amplitude ship motions can lead to a pronounced unsteady behavior of the propeller, which might yield large thrust and loading variations. Viscous CFD simulations of geometrically resolved propeller flows behind a floating vessel in seaways are still afflicted with prohibitive computational expenses. On the contrary, methods based on the potential theory are not able to predict the wake flow with the required level of accuracy.

To overcome the dilemma, the development of a close coupling strategy between inviscid and RANS techniques has been put into the focus of the present research. The effort aims to retain the merits of both strategies at modest computational and work-flow costs. Similar to former coupling attempts, the viscous method is used to determine the approach flow towards the propeller, while the inviscid method is used to predict the forces exchanged by the propeller and the fluid. The latter are

used to derive the body forces which mimic the influence of the propeller on the viscous flow field. A coupled approach greatly simplifies the viscous mesh generation for the propeller regime and supports efficient studies on blade-shape influences. No rotating mesh is required for coupled simulations and significantly smaller viscous grids can be used - a feature which is of particular relevance for unsteady simulations involving multiple time scales. Notice that the present coupling strategy is inherently unsteady and no circumferential averaging is applied.

The present research is concerned with partially submerged, surface-piercing propellers. Thus, the free surface has been included into the coupling procedure. Accordingly, the time accurate position of the free-surface is predicted by the viscous method and transferred to the inviscid method by means of a truncated Fourier-series representation.

The paper is structured as follows: the second and third sections are devoted to the viscous and inviscid methods; the fourth section outlines the rationale of the coupling strategy; section five refers to simple validation cases; subsequently, the application of the coupling method for a transient propeller flow exposed to an inhomogeneous wake field is reported; and finally, the paper ends with an outline of the conclusions and future aims.

2 VISCOUS METHOD

The present study utilizes the viscous flow solver *FreSCO*⁺, a spin-off of the *FreSCO* solver (Rung et al 2009) that was jointly developed by the Hamburg University of Technology, the Hamburg Ship Model Basin (HSVA) and the Dutch Maritime Research Institute (MARIN).

The segregated algorithm is based on the strong conservation form of the momentum equations and employs a cell-centered, co-located storage arrangement for all transport properties. Structured and unstructured grids with arbitrary polyhedral cells or hanging nodes can be used. The implicit numerical approximation is second-order accurate in space and time. Integrals are approximated using the conventional mid-point rule. The solution is iterated to convergence using a SIMPLE-type

pressure-correction scheme. Various turbulence-closure models using statistical (RANS) or scale-resolving (LES, DES) approaches are available. Two-phase flows are modeled by interface-capturing methods based upon the Level-Set or Volume-of-Fluid (VOF) technique. In the presented study, a VOF-method is used. To obtain the solution for the linear equation systems, methods offered by the PETSc library are employed. The algorithm is parallelized using a domain-decomposition technique based on a Single Program Multiple Data (SPMD) message-passing model, i.e., each process runs the same program on its own subset of data. Inter-processor communication employs the MPI communications protocol. Load balancing is achieved using the ParMETIS partitioning software.

3 INVISCID METHOD

The potential-flow method *panMare* (Abdel-Maksoud et al 2010) is developed at the Hamburg University of Technology. It is a Boundary-Element method, i.e., only the geometric-boundaries and (if existing) the water free surface are discretized. A set of linear equations is solved to calculate the forces and velocities. The BEM is based on the solution of the Laplace equation $\Delta\Phi = 0$, where Φ is a velocity potential. This potential is a linear combination of several sources and doublets which are distributed as NB quadrilaterals on the surface of the body. The circulation generated by the propeller develops as a sheet of NW doublets into the trailing flow. The equation for the velocity potential Φ at the location \mathbf{x} becomes:

$$\Theta(\mathbf{x}) = -\frac{1}{4\pi} \left(\sum_{j=1}^{N_B} \sigma_j \int_{A_j} \frac{1}{r_j(\mathbf{x})} ds + \sum_{j=1}^{N_B+N_W} \mu_j \int_{A_j} \mathbf{n}_j \nabla \frac{1}{r_j(\mathbf{x})} ds \right) + \Theta_\infty$$

with σ being the source strength, μ_j being the dipole strength, \mathbf{r}_j being the distance between \mathbf{x} and panel j , and A_j being the area of panel j . Using the Neumann boundary condition $\mathbf{n}\mathbf{v} = 0$, N_B linear equations can be derived, with \mathbf{n} being the normal vector pointing into the flow and \mathbf{v} the velocity at a point on the surface. As the system does not have a unique solution, the sources need to be prescribed by another condition. This is done by an equation where σ is related to the free stream velocity \mathbf{v}_∞

$$\sigma = -\mathbf{n}\mathbf{v}_\infty$$

Further, the strength of the trailing vortices is defined by the linear Kutta condition applied on the trailing edge. For calculating the forces acting on a propeller behind a ship, arbitrary distributions of inflow velocities (e.g., non-axisymmetric) can be used. When the inflow velocities are axisymmetric a quasi-stationary method can be applied, where blade forces are calculated for different angular positions.

4 COUPLING STRATEGY

In the present approach, the propeller is not geometrically resolved in the viscous flow solver, but modeled by rotating sets of volumetric body forces for each blade. In accord with former coupling strategies (Zawadzki et al 1997), the viscous method is used to calculate the inflow condition of the propeller, while the inviscid method is used to predict the propeller forces. The corresponding reaction forces are employed as body forces in the viscous approach.

The coupling approach is based on the exchange of two properties, i.e., the transfer of inviscid propeller-induced body-forces to the viscous solver and the transfer of the (reduced) effective wake velocities to the inviscid solver. As regards the implementation, two details of the coupling procedure related to the (a) spatial and (b) temporal transfer of information are of specific interest. The former issue is associated to mapping techniques between two grids of substantially different nature, whereas the latter issue is concerned with explicit, implicit or semi-implicit time advancing techniques.

The viscous velocity distribution is extracted in a plane typically located 0.1D-0.2D upstream the propeller. As depicted by Figure 1, the respective data is mapped onto a predefined set of structured, locations in a circular domain (specified by corresponding angular and radial positions).

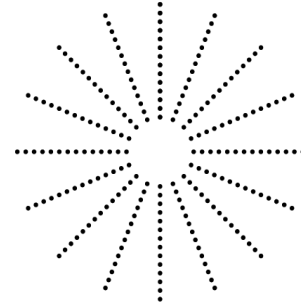


Figure 1: Example of locations used for the velocity transfer.



Figure 2: Illustration of exemplary body forces in the blade region of the RANS mesh (approx. 800 cells are involved).

The spatial transfer of body-forces from the potential flow solver to the viscous solver follows a different route. Since one force per grid-panel is transferred, the forces of the pressure- and suction-side of the blade are calculated separately. The forces are then distributed to the adjacent fluid cell centers of the RANS mesh as volumetric body

forces (cf. Figure 2). Although the grids of the viscous and the inviscid method are significantly different, in particular with respect to the grid density, the mapping procedure maintains force conservation. It utilizes a cell-search algorithm that connects each panel to the closest cell center and the corresponding neighboring cells in a conservative way.

4.1 Baseline Coupling Algorithm

The baseline algorithm is restricted to deeply submerged propellers. The inviscid solver requires a reduced effective wake field to predict the propeller-induced forces acting on the fluid. The reduced wake velocities comprise the viscous flow velocities reduced by the induced velocities, obtained from the inviscid method. Accordingly, two different coupling modi, i.e., an explicit and an implicit procedure, have been implemented. A third semi-implicit approach is conceivable but not reported in greater detail here. The strategies differ by means of the level of time-synchronization between the involved three velocity fields and the inviscid forces.

Figure 3 illustrates the flow charts of the two realized coupling modes. The first mode pertains to an explicit coupling algorithm and involves only one coupling cycle per time step.

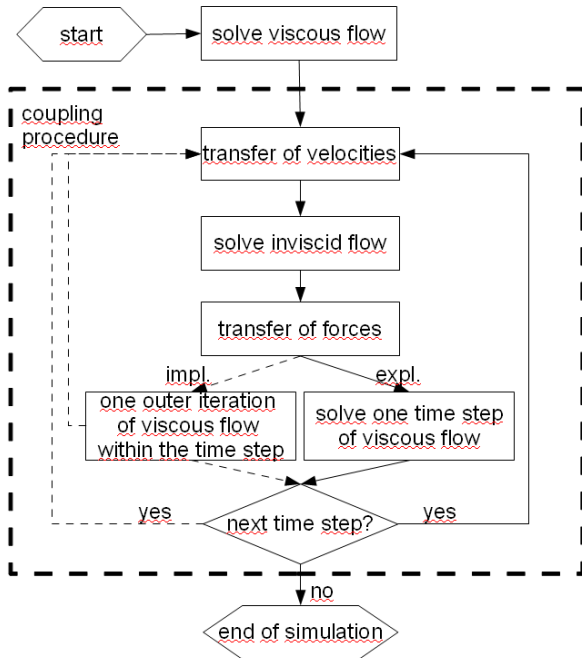


Figure 3: Flow-chart of the employed coupling algorithm.

At the beginning of each coupling cycle, the viscous velocity distribution upstream of the propeller plane is transferred to the inviscid method. The explicit procedure (cf. solid lines in Figure 3) uses the viscous wake velocities of the previous time step upstream the new blade locations and continues with the calculation of an induced velocity field from the former solution of the inviscid method. Subsequently, the induced inviscid velocities are subtracted from the viscous wake velocities

to obtain the fully explicit representation of the propeller approach flow. The algorithm proceeds with the solution of the equation system inside *panMare* to determine the propeller forces. The force distribution is transferred to the viscous method and the time step is finalized by the solution of the governing equations in *FreSCO*⁺.

The second mode (dashed lines) refers to an implicit approach. It involves multiple coupling cycles in each time step. Here, the inviscid solution is embedded into the outer iteration process of the segregated viscous solver. For each time step, a sequence of outer iterations is performed in line with the description for the explicit mode. An updated time-accurate viscous velocity distribution is transferred to the BEM in every outer iteration of *FreSCO*⁺. The reduced effective and induced wake velocities employed by *panMare* are therefore also determined in a time accurate manner. The solution advances in time after a converged solution is achieved in both solvers.

A third technique might only iterate the induced velocities to convergence. Using the former inviscid solution as an initial guess for the induced velocities, the latter are updated for a sequence of new inviscid solution. The respective effective wake is thus composed from the former viscous wake and the present induced velocities. The two baseline methods are still explicitly coupled which reduces the global effort. Although the third approach seems debatable due to the obvious inconsistencies, it can yield significant performance benefits over the fully explicit strategy.

4.2 Extension for Free-Surface Flows

In order to extend the coupling procedure to free-surface flows, the position of the free surface must be transferred to the BEM. Inside the BEM, the free-surface is modeled as an inviscid wall. Because the required grid density differs significantly between the viscous and the inviscid solver, independent grids connected to different data structures have to be supported.

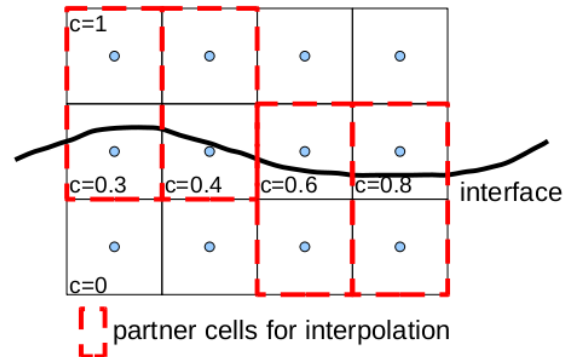


Figure 4: Reconstruction of the interface position in the viscous VOF-method.

As mentioned in Section 2, a volume of fluid method is used to capture the free surface position inside the RANS-solver. Thus, the interface between water and air is reconstructed by an interpolation of the mixture fraction

$c = 1$ refers to air and $c = 0$ pertains to water - as illustrated in Figure 4.

The aim of the present approach is to impose no additional restriction to the two baseline methods and their respective numerical grids. The mapping is thus realized in a two-step approach, which utilizes an analytical intermediate description of the free-surface. Moreover, a ruptured inviscid free-surface representation is undesirable within the inviscid approach. Thus, the inviscid representation has to maintain a fair level of geometric continuity. The approach inherits three steps which are all performed inside the viscous method:

1. **Reconstruction Step:** Reconstruction of the interface from the computed mixture fraction. This results in an unstructured representation of the free surface on the viscous grid. The resulting interface might be ruptured or contain splashes.
2. **Mapping Step:** Interpolation of the unstructured free surface data on a regular grid.
3. **Transformation Step:** Fourier transformation of the mapped, regular-grid representation of the interface. The use of a truncated Fourier series should provide a sufficiently smooth inviscid interface representation.

The Fourier transformation employs two-dimensional cutting planes along the main flow direction and only the Fourier coefficients are passed to the BEM. Typically 10-15 terms are considered in the truncated Fourier series. The height of the free surface can subsequently be determined at arbitrary planar positions of the panel grid in *panMare*. The position of the free surface is updated in each coupling cycle when a new distribution of velocities is transferred.

5 VALIDATION

5.1 Influence of the Coupling Strategy

This subsection is devoted to a comparison between the implicit and explicit coupling approach. Emphasis is given to the attainable computational efficiency by means of the time-step size, the number of iterations used to determine the induced velocities and the amount of outer iterations inside *FreSCO*⁺. These principal parameters govern the computational effort and the convergence behavior. For this purpose, a deeply submerged propeller in open water conditions has been computed. More details about the test case can be found in Section 6.1.

In a first comparison, the explicit and implicit algorithm are used to compute the thrust coefficient of a propeller at an advance coefficient of $J = 0.9$. The temporal evolution of the thrust coefficients are shown in Figure 5. Both methods show very similar results. The propeller revolution was discretized with 72 time steps. The time step was identical for the explicit and implicit calculations. The larger computational effort for the implicit algorithm does not result in a premature

convergence. This is attributed to the stationary character of the investigated test case. To reduce the computational effort of the implicit algorithm, the iterations should be monitored by means of the actual objective function, i.e. the predicted thrust. Figure 6 displays the thrust prediction for three consecutive time steps.

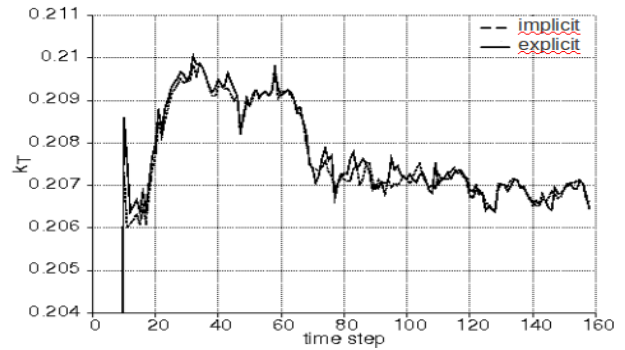


Figure 5: Comparison of the computed thrust coefficient obtained from the implicit and explicit coupling algorithm.

The beginning of each time step is marked by a solid vertical line, while the dashed line represents the outer iteration where the relative thrust change between two iterations falls below 1%. We thus limit the amount of outer iterations to this threshold which reduces the amount of iterations to 5 in the present case.

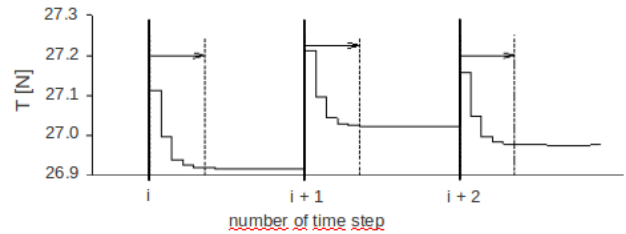


Figure 6: Convergence behavior of the implicit coupling algorithm within three subsequent time steps (dashed lines indicate the fifth outer iteration).

The difference between the values for the propeller induced velocities calculated by both solvers is about 0.1 %.

5.2 Free-Surface Transformation

Prior to the application examples, the accuracy of the free-surface transformation is scrutinized with the aid of a simple 2D hydrofoil case. The computations refer to the flow over a submerged NACA0012 hydrofoil. The case was experimentally investigated by Duncan (1983). The foil operates at a Froude number of $F_n = v/\sqrt{gc} = 0.567$ and it is located at a distance of $d/c = 1.034$ below the free-surface.

The test case reveals a stationary flow around the hydrofoil featuring a steady wave-field. Figure 7 illustrates the predicted viscous results for a geometrically resolved hydrofoil using laminar flow conditions at $Re = 1.6 \cdot 10^5$ on a 2D mesh with approximately 50.000

hexahedral cells.

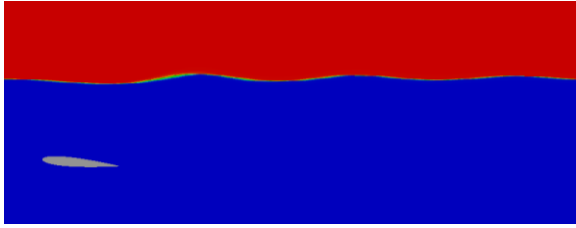


Figure 7: Surface elevation above the Duncan hydrofoil ($F_n=0.567$, $Re=1.6 \cdot 10^5$; resolved viscous flow solution).

The predicted wave field is used to validate the inviscid representation of the free surface. In Figure 8 the free surface obtained from the truncated series expansion (indicated by *Fourier*) is compared to the actually predicted free surface elevation (indicated by *FreSCo⁺*).

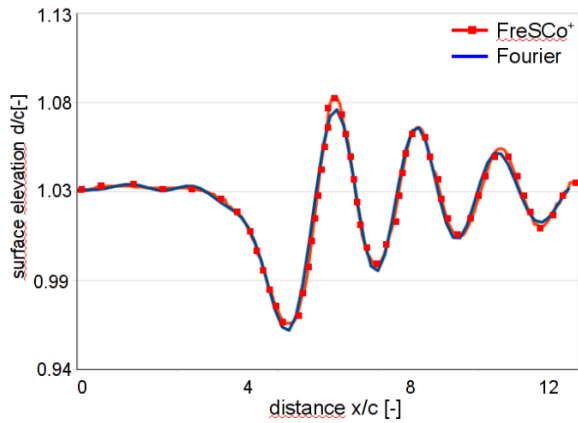


Figure 8: Comparison of the predicted free surface heights. The red line represents the original viscous results, the surface elevation obtained from the Fourier series is displayed by the blue line.

The employed Fourier series involves 12 coefficients. Only small deviations between the original result (indicated by the red line) and the reconstruction of the interface (indicated by the blue line) occur. Thus, the elevation of free surface is transferred to the BEM with a sufficient amount of accuracy.

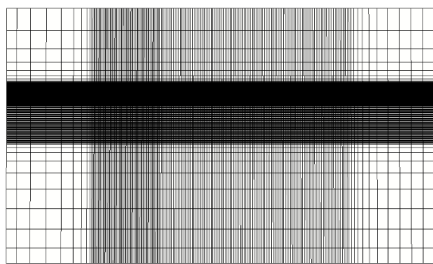


Figure 9: Computational grid employed for the coupled simulation of the Duncan hydrofoil.

Coupled simulations have been performed for the same case. Accordingly, the geometry of the hydrofoil is only modeled in the BEM and the viscous method uses a

simple 2D-Cartesian grid of 45.000 hexahedral cells as outlined in Figure 9. Since the test case refers to a steady state solution, the employed coupling technique is not crucial. The converged solution of the coupled computation shows the stationary wave field displayed in Figure 10. The figure also shows the distribution of body forces, colored with the magnitude of the imposed body-force vector.

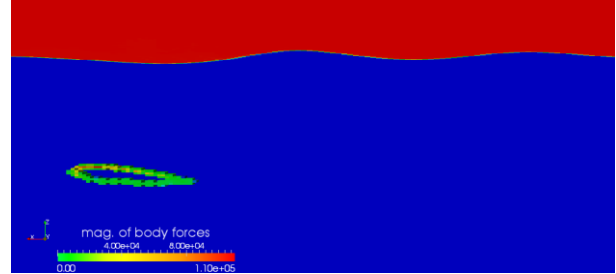


Figure 10: The force distribution of the foil generates a stationary wave field.

A comparison between the predicted surface elevations obtained from the coupled approach and the geometry-resolving viscous simulation can be found in Figure 11. The elevations predicted by the coupling algorithm - indicated by the red closed squares - are slightly lower than the results from the viscous computation. However, an encouraging overall agreement between both results is seen.

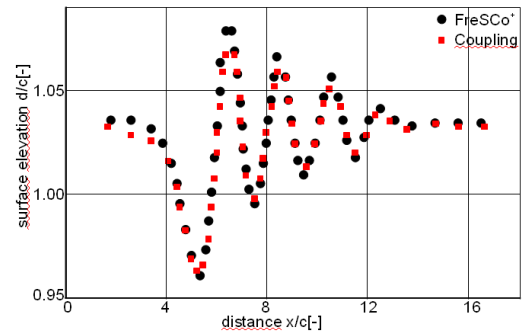


Figure 11: Comparison of the predicted free surface elevation obtained from the resolved hydrofoil simulations (black - *FreSCo⁺*) and the coupled simulations (red - *Coupled*).

6 PROPELLER FLOW APPLICATIONS

6.1 Propeller in Open Water conditions

The first application example refers to open-water calculations of a propeller, where model-scale experiments were performed by MARINTEK under the aegis of PROPSEAS (Kozłowska et al., 2011). The investigated propeller has a diameter of $D = 0.2m$ and operates with $n = 18$ revolutions per second. Different advance coefficients are achieved by a variation of the inflow velocity. The numerical grid of the propeller used in the BEM consists of 544 panels per blade (cf. Figure 12 - left). Figure 12 (right) displays the propeller regime of the viscous grid. About 2.500 of 15.000 control

volumes in the propeller disc are subjected to body forces. The Reynolds number based on the chord length at $r/R = 0.7$ and the resulting velocity at the propeller blade reads $Re = 0.5 \cdot 10^6$. The flow is considered fully turbulent using the standard $k-\omega$ turbulence model.

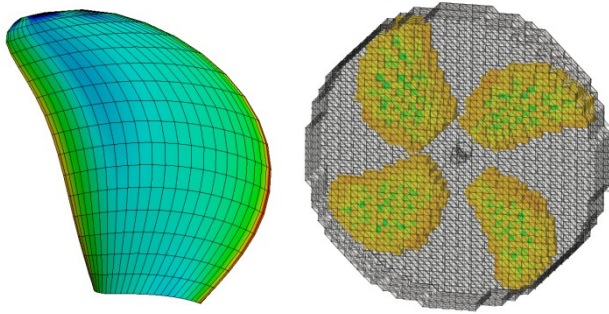


Figure 12: Numerical grid and resulting pressure distribution for the BEM simulation (left). FV-grid in the propeller disc (right). Only cells at the actual blade positions contain body forces (colored).

An open-water diagram of the test case can be found in Figure 13. Results of the coupling procedure are shown with dashed black lines, while the results obtained from the BEM-solver *panMare* are shown with blue dotted lines. Comparison is made to measurements done by MARINTEK indicated by the solid black curves. A fair agreement is seen for the predicted thrust values, while larger deviations occur for the torque values. A possible reason for this deterioration can be the empirical determination of the surface-friction losses inside *panMare* which have a larger influence on the torque. Furthermore small deviations between the coupled results and *panMare* can be obtained. This might be influenced by different resolutions of the pressure peak at the leading edge between the involved methods.

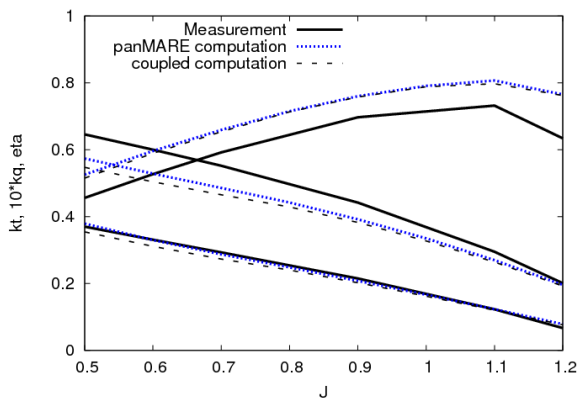


Figure 13: Open water diagram; Comparison between measurements, BEM and coupled simulation.

6.2 Pushing Pod-Propeller

The second application example refers to a thruster configuration with a pushing propeller, investigated by Koushan (2006, 2009). The propeller has a diameter of $D = 0.25m$ and operates at an advance coefficient of $J = 0.9$. It operates in a non-uniform wake-field behind

the strut. The test case should illustrate the ability of the coupling algorithm to capture localized and unsteady effects. The BEM uses 690 panels per blade. The viscous flow ($Re = 0.5 \cdot 10^6$) is treated fully turbulent using again the standard $k-\omega$ turbulence model in conjunction with a high- Re formulation for the wall boundary conditions. The viscous mesh employs approximately 300.000 unstructured hexahedral cells. To accurately capture all unsteady effects, a rather small time-step - corresponding to 3° of a revolution - is chosen.

The housing of the thruster, as well as the propeller hub are geometrically modeled in the viscous method, while the exact blade geometries are only present in the BEM. The viscous configuration comprising the hub geometry and the body-force representation of the blades is displayed in the upper part of Figure 14. The figure shows the non-dimensional pressure distribution on the thruster housing and in the positions of the blades for three instants in time. The pressure distribution in the blade regions is a result of the body-force distribution. Overall larger blade-related pressure gradients are obtained in the upper section behind the strut and the maximum pressure on the upper blade is further increased while the blade passes the wake of the strut. The lower part of the figure shows the corresponding pressure distribution on the blade obtained with *panMare*. The figure depicts a qualitative good agreement between both methods.

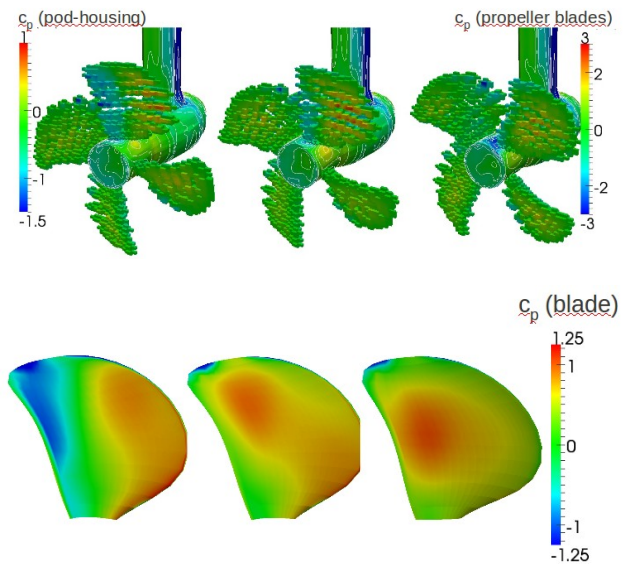


Figure 14: Top: Configuration used in FreSCo+. The blades are modeled with body forces. The figure shows the pressure distribution on the pod-housing and in the cells, where the propeller blades are located. Bottom: Pressure distribution on one blade computed with *panMare* for the same instants in time. The corresponding blade position refers to 0° , 22° and 45° respectively. Note, different scales are used to cover the range of the pressure variations.

The challenge of the case refers to the narrow-banded wake field aft of the strut.

Figure 15 displays the results of the nominal (right) and the effective wake (left). The nominal wake features large

gradients of the propeller inflow. Directly downstream of the pod ($X/D = 0.24$; measured from the propeller plane), the axial velocity is reduced up to 10% of the inflow velocity in the upper position of the wake field. The resulting variations of the velocity magnitude and blade angle-of-attack refer to approximately 30% and 10° respectively (cf. Figure 16). As can be seen from Figure 15, the effect of the strut is less pronounced if the distance from the pod is increased ($X/D = 0.16$). The right side of the figure also reveals a low-momentum area above the hub which results from a horseshoe vortex emanating from the pod-strut junction. Large tangential velocity components are generated beneath the strut. Hence, a propeller blade passing the upright position operates at a smaller advance coefficient compared to the other blades.

The left side of Figure 15 displays the result for the coupled simulations. Analogues to the before described results low axial momentum can be observed behind the strut ($X/D = 0.24$), while in the plane closer to the propeller plane ($X/D = 0.16$) an influence of the propeller induced velocities is clearly visible.

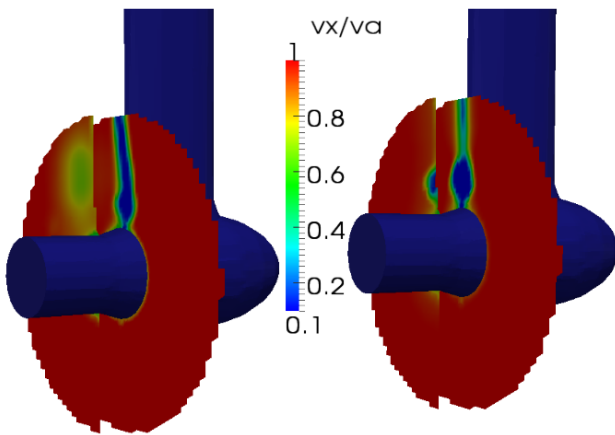


Figure 15: Computed wake field in two axial-planes upstream the propeller plane ($X/D=0.16$, and $X/D=0.24$ – measured from the propeller plane). The left picture shows the wake with an operating propeller, while the right picture refers to the nominal wake of the unpropelled case.

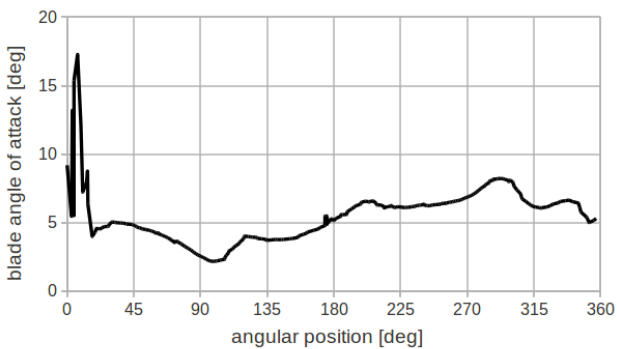


Figure 16: Variation of the blade angle-of-attack for different angular positions.

The influence of the strut and the propeller can also be found in Figure 17. The figure outlines the temporal

evolution of the normalized axial velocity v_x/v_a at a radius of $r/R = 0.7$ for four different locations located $X/D = 0.16$ upstream of the propeller plane. Displayed results are confined to one revolution period.

The first curve (labeled 1) denotes the upright position, while the other curves refer to the lowest (labeled 3), the starboard (labeled 2) and portside (labeled 4) positions. Of course, the lowest values for the axial velocity can be found behind the strut, while values close to the inflow velocity can be found at the other positions. Mind, that the figure shows one of the first revolutions. In this stage, the simulation still reflects significant initial transient influences and discrepancies between the beginning and the end of the computation can thus be observed.

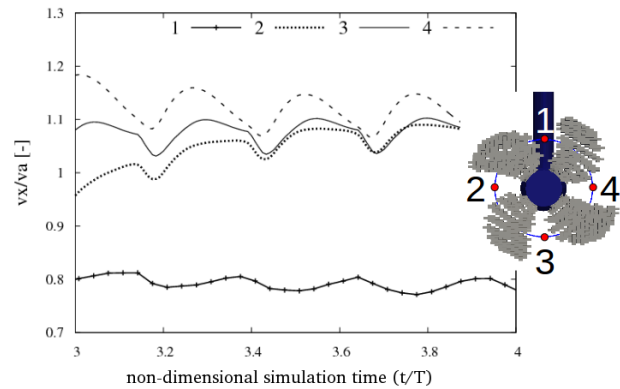


Figure 17: Axial velocity during one revolution at $x=0.16D$ in front of the propeller plane. The single curves refer to velocities at different angular positions at a radius of $r/R=0.7$ (see right figure).

The thrust coefficients for one revolution of a single blade (dotted line) and the complete propeller (solid line) are shown in Figure 18. The thrust variations due to the non-uniform wake field over one propeller revolution are obvious. The low momentum region behind the strut results in higher forces on the blades.

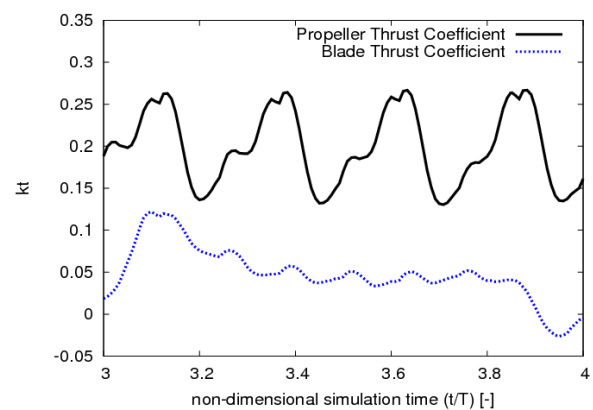


Figure 18: Calculated thrust coefficient for one blade (dotted line) and full propeller (solid line).

The thrust and torque coefficients of the propeller are quite regular and have predicted mean values of $k_t = 0.199$ and $k_q = 0.382$. The corresponding measured

values for the propeller in open water read $k_t = 0.193$ and $k_q = 0.387$ (Califano et. al.). Thus, a fair predictive accuracy has been obtained.

7 CONCLUSION

The development of a close-coupling algorithm between an inviscid method and a RANS method is presented. Although further development of the BEM is necessary to improve the quality of the predicted torque coefficient, an encouraging overall accuracy has been observed.

The present coupling method can capture localized and transient effects associated to small details of the wake-field. It is thus applicable to a variety of practical applications, e.g., pushing pod propeller studies or pressure fluctuations on rudders or hulls.

The coupling algorithm is robust and shows a favorable convergence behavior. It supports the use of coarse and simple hexahedral viscous grids in the propeller regime which significantly reduces the simulation time compared to geometrically resolved viscous propeller-flow simulations.

Future work will address free-surface influences for simulations of self-propelled ships in seaways. For such simulations, the time-step size is governed by the resolution of the floating motion and not the revolutionary speed of the propeller which drastically reduces the simulation effort.

ACKNOWLEDGEMENT

This work was carried out as a part of the MARTEC Research Project PROPSEAS, founded by the German federal Ministry of Economics and Technology (BMWi) and the Research Council of Norway. Partners in the project are MARINTEK, Rolls-Royce, Norwegian University of Science and Technology, Hamburg University of Technology, University of Duisburg-Essen, Germanischer Lloyd, Farstad Shipping and Develogic GmbH.

REFERENCES

- Abdel-Maksoud, M., Steden, M. & Hundemer, J. (2010). 'Design of a Multi-Component Propulsor'. 28th Symp. on Naval Hydrodynamics, Pasadena, USA.
- Califano, A. & Steen, S. (2009). 'Analysis of different propeller ventilation mechanisms by means of RANS simulation'. Proceedings of the first International Symposium on Marine Propulsors, Trondheim, Norway.
- Duncan, J. H. (1983). 'The Breaking and non-Breaking Wave Resistance of a two-dimensional Hydrofoil'. Journal of Fluid Mechanics **126**, pp. 507-520.
- Koushan, K., Spence, S. & Hamstad, T. (2009). 'Experimental Investigation of the Effect of Waves and Ventilation on Thruster Loadings'. Proceedings of the first International Symposium on Marine Propulsors, Trondheim, Norway.
- Koushan, K. (2006). 'Dynamics of Ventilated Propeller Blade Loading on Thrusters Due to Forced Sinusoidal Heave Motion'. 26th Symp. On Naval Hydrodynamics, Rome, Italy.
- Kozłowska, A., Wöckner, K., Steen, S., Rung, T., Koushan, K. & Spence, S. (2011). 'Numerical and Experimental Study of Propeller Ventilation'. Proceedings of the second International Symposium on Marine Propulsors, Hamburg, Germany.
- Rung, T., Wöckner, K., Manzke, M., Stück, A., Brunswig, J. & Ulrich, C. (2009). 'Challenges and Perspectives for Maritime CFD Applications'. Jahrbuch der Schiffbautechnischen Gesellschaft **103**.
- Zawadzki, I., Fuhs, D. & Gorski, J. (1997). Integration of a Viscous Flow RANS Solver with an Unsteady Propulsor Force Code. Cardrock Division Naval Surface Warfare Center.